An assessment of event-based imaging velocimetry for dimensionality reduction in turbulent flows

Luca Franceschelli[1,*], Marco Raiola[1], Christian E. Willert[2] and Stefano Discetti[1]

1: Department of Aerospace Engineering, Universidad Carlos III de Madrid, Avda. Universidad 30, Leganés, 28911, Madrid, Spain
2: DLR Institute of Propulsion Technology, German Aerospace Center, 51170 Köln, Germany

*Corresponding author: lfrances@ing.uc3m.es

Keywords: PIV, event-based velocimetry, POD, dimensionality reduction, flow control.

ABSTRACT

This study investigates the feasibility of using neuromorphic event-based vision (EBV) camera for low-order modelling, a key enabler for real-time flow control. A synchronized experiment with simultaneous Event Based Image Velocimetry (EBIV) and Particle Image Velocimetry (PIV) is performed on a submerged water jet flow at Re = 2600. Flow statistics, spectral content, and reduced-order modeling capabilities using Proper Orthogonal Decomposition (POD) are assessed. Velocity fields are computed via standard PIV processing and compared after interpolation onto a common grid. The analysis reveals good agreement in jet flow statistics and spectra between EBIV and conventional PIV, with differences observed in the power spectral density (PSD) for high frequencies ($St > 1.5$) due to higher noise levels in EBIV data. Nonetheless, most of the spectral content is correctly captured by the EBIV. EBIV successfully identifies dominant flow structures and spectral distribution of energy. The correct identification of temporal modes confirms EBIV's potential for flow control applications based on reduced order models. Despite minor discrepancies downstream of the jet in the Low Order Reconstruction (LOR) analysis, attributed to EBIV's challenge in accurately reconstructing broad-spectrum turbulent regions, the technology proves promising for real-time imaging-based flow control.

1. Introduction

Particle Image Velocimetry (PIV) is a highly-consolidated tool for flow diagnostics. Its capacity for offering quantitative flow visualization provides users with valuable physical insights into the studied flow case, surpassing the capabilities of other techniques. However, the complexity and processing time associated with PIV, both in terms of image capture and analysis, have hindered so far its use as a "sensor" for real-time control of fluid flows. The data size is the main bottleneck. Techniques such as thermal anemometry, laser Doppler Velocimetry or fluctuating pressure

measurements with microphones, instead, enable the measurement of single-point flow properties at frequencies that can easily extend into the kHz regime. Depending on the control purpose, actuation decisions can be made by exploiting previous knowledge of the flow dynamics and the expected effect of the actuation. On the downside, such techniques are invasive and do not allow full-state estimation. The primary advantage that PIV brings is its ability to provide full-field, topological information in a non-intrusive manner, enhancing actuator effectiveness. Furthermore, PIV data can be used to build tailored low-order models, which can be used to reduce the dimensionality of the control problem and identify compact (and fast-to-compute) actuation strategies. Previous studies have ventured into this possibility (Willert et al., 2010, and Siegel et al., 2003, for example), achieving time delays on the order of 100 ms from image acquisition to processing. The primary source of time delay is identified as the image acquisition process.

In this sense, neuromorphic sensors, also referred to as event-based vision (EBV) or dynamic vision sensing (DVS), provide a technological novelty, with the potential to significantly reduce the inherent time delay introduced by the image acquisition and processing of conventional cameras. In conventional cameras, exposure and read-out time are globally controlled and set for the whole sensor. On the other hand, in EBV each pixel operates as an independent asynchronous temporal contrast change detector. A pixel triggers an event only when the integral of the temporal contrast, represented as the temporal variation of the logarithmic intensity

$$C_{\text{temporal}} = \frac{1}{I(t)}\frac{dI(t)}{dt} = \frac{d}{dt}\ln[I(t)], \tag{1}$$

surpasses a predefined threshold in comparison to the previous event (Lichtsteiner et al., 2008; Posch et al., 2014). In this context, $I(t)$ denotes the photo-current generated by the photodiode, which is proportional to the pixel illumination. The sensor output is a continuous asynchronous stream of events, consisting of the activated pixel address, the time-stamp of the event referred to the global clock of the sensor and the polarity, indicating whether the event is a positive or negative contrast change. The event triggering definition and relation to the logarithmic change of intensity allows these sensors to reach a dynamic sensor range in the order of 120 dB. Such sensitivity at low-intensity levels extends its applicability also in situations where the amount of light is not typically enough for conventional PIV measurements. It also makes the sensor dependent only on local intensity changes, despite global illumination non-uniformity or light reflections, a cumbersome issue on most experimental PIV set-ups. Considering the temporal resolution of today's DVS, in the order of 100 μs, flow field events can be recorded at the analogous of a framing frequency for conventional high-speed CMOS-based cameras exceeding several kHz, but with a significantly reduced data volume. The ability to access volumetric flow field information at a sufficiently high frequency, with a "slim"-enough stream of events to be easily and rapidly processed, together with the high sensitivity to contrast changes, paves the way to the possibility for PIV-based real-time closed-loop control in turbulent flows.

However, the use of these sensors is subject to certain limitations. The arbiter, i.e. the designated circuit element responsible for associating each event with the global sensor clock, can effectively process events only up to a maximum number of simultaneous events. This limitation consequently constrains the speed of the flow field case and the dimension of the resolved volume. Furthermore, the event sensor's pixels are characterized by latency (i.e. response time), which hinders the temporal accuracy of event detection, resulting in information loss. In the context of PIV/PTV applications, a notable loss of accuracy is observed due to the inherent impossibility of achieving sub-pixel accuracy, stemming from the binary event definition as ON/OFF states. To a certain extent, this can be mitigated using the equivalent of multiple frame PIV processing schemes Willert (2023).

Gallego et al. (2022) present comprehensive insights into the current state of event-based vision, encompassing its diverse applications and the associated data processing landscape. In the field of fluid mechanics, Willert (2023) successfully addressed challenges related to event rate limits and sensor inherent time-latency by employing a pulsating laser as a light source. This development, known as pulsed event-based imaging velocimetry (*pulsed-EBIV*), is implemented and referred to as EBIV in this work. The results, employing typical PIV-processing algorithms across various test cases, align well with measurements obtained using conventional PIV cameras. Given the asynchronous and independent working principle of EBV sensors, PTV-based approaches have also been investigated. Recently, Rusch & Rösgen (2023) integrated a real-time 3D event-based PTV acquisition system into their wind tunnel, demonstrating its ability to reconstruct particle trajectories in diverse industrial applications. In recent years, there has been notable progress in the implementation of EBV-based stereoscopic PIV (Wang et al., 2020), and optical-flow-based methods leveraging EBV have been explored (Shiba et al., 2023).

In view of the future application of EBV cameras as sensors for closed-loop flow control, this study aims to initially assess the reduced-order modeling capabilities of EBV cameras, comparing them with conventional sCMOS sensor-based cameras. We aim to address the following research questions: is EBIV mature enough to establish a suitable data-driven basis with a reduced amount of samples? Is the basis of a sufficient quality for estimation of the dynamics of a flow? In this work, the reduced-order modeling capability of an event-based camera is assessed and compared to that of a conventional PIV camera. A synchronized experiment using these two types of image acquisition technologies is performed on a jet flow. The resulting flow statistics, spectral content, and modes from Proper Orthogonal Decomposition (POD, Lumley 1967) are compared.

2. Experimental Set-up

The comparative analysis between PIV and EBIV is conducted on a submerged water jet flow case. A synchronized acquisition was carried out using an sCMOS camera and an EBV camera,

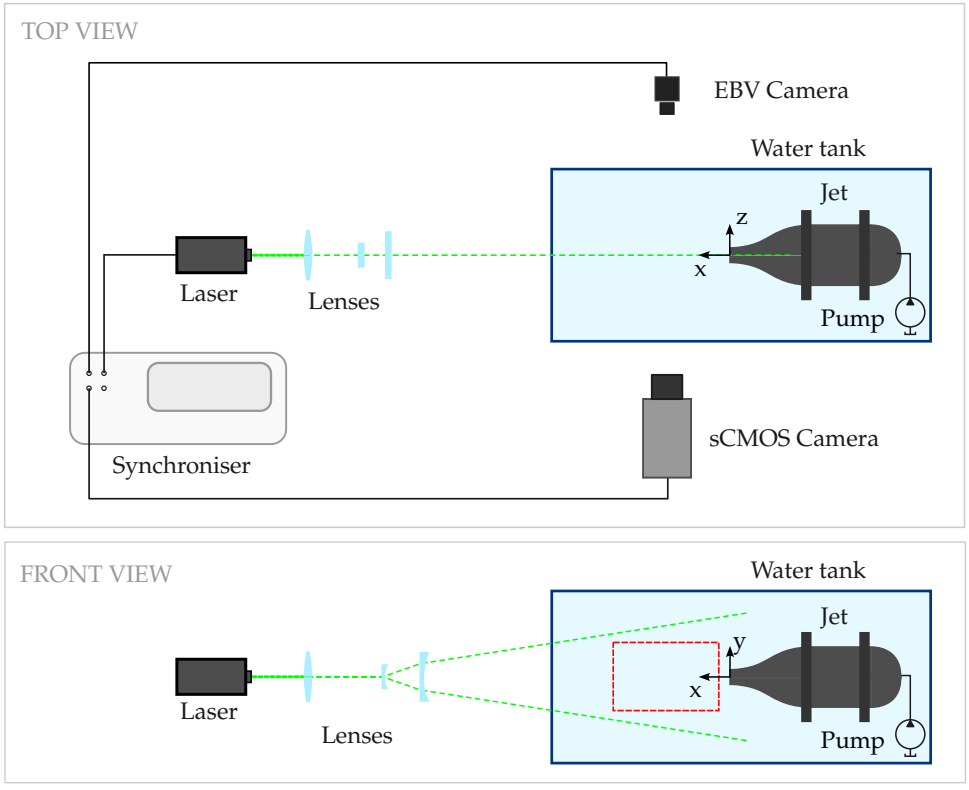

Figure 1. Submerged water jet-flow, sketch of the experimental set-up: in red the common region onto which the obtained velocity fields are interpolated.

positioned facing each other. The field of view (FOV) and image magnification is closely matched to ensure an objective comparison of the results obtained with the two systems. The jet nozzle, with an exit diameter $D = 20$ mm, is operated at a bulk velocity of approximately $U_j \approx 0.13\,\mathrm{m/s}$, resulting in a turbulent jet flow at a Reynolds number of $Re \approx 2600$. The jet is contained within an $80 \times 60 \times 40\,\mathrm{cm}^3$ water tank and seeded with polyamide particles of $56\,\mu\mathrm{m}$ diameter. Illumination on the symmetry plane of the jet is provided by a pulse-width modulated laser, originally designed for wood engraving (LaserTree LT-40W-AA), with a power of $5\,\mathrm{W}$. The laser beam is shaped as a thin laser sheet through a set of lenses, reaching a thickness of around $1 - 2\,\mathrm{mm}$ at the nozzle position. The laser is controlled with a pulse generator: the pulse width is set at $1\,\mathrm{ms}$, and the time interval between two consecutive laser pulses is $dt = 10\,\mathrm{ms}$, corresponding to a frequency $f = 100\,\mathrm{Hz}$. The pulse generator also provides the acquisition trigger signal for the PIV camera and the reference trigger signal for the event-based camera. In the event-based camera, this signal serves as a reference point within its data stream, ensuring temporal alignment between the two camera systems and thereby facilitating coherent data acquisition and analysis. The experimental setup is illustrated in Fig. 1.

For the conventional PIV camera acquisition, the flow field is captured using an sCMOS camera (Andor Zyla) with a 5.5 megapixels sensor and a pixel pitch of $6.5\,\mu\mathrm{m}$. The field of view has been

cropped to a resolution of 1500×720 pixels, covering a domain of approximately $8 \times 3.8D$. A time-resolved sequence consisting of $4{\cdot}10^4$ samples is captured.

EBIV measurements are performed using an EBV camera (Prophesee EVK4), featuring the Sony IMX636 sensor with a resolution of 1280×720 pixels and a square pixel pitch of $4.86 \times 4.86\,\mu m$. Under nominal conditions the pixel latency is below $100\,\mu s$. The imaged flow field covers a domain of approximately $7D \times 4D$. The acquisition software allows for user-defined tuning of event sensitivity. However, for the purpose of providing general considerations about this new technology, no tuning has been implemented, leaving room for potential improvements in the quality of the acquired data. In this case, the acquisition consists of a event stream of a few minutes. The acquired data stream has an average event-data rate of approximately $60\,Mev/s$ (mega-events per second), corresponding to a data rate of approximately $130\,Mb/s$. Following the procedure proposed by Willert (2023) the event stream is then partitioned to the reference trigger signal to obtain a set of $4{\cdot}10^4$ pseudo-snapshots.

Fig. 2 shows a histogram related to the registered events in time. Green and blue dashed lines are included in the figure to indicate the beginning and end of the laser pulse, respectively. The event burst occurs as the laser is triggered. A synthetic snapshot is then generated accumulating all the positive events (Polarity = 1) registered from the beginning of the laser pulse and a user-defined *accumulation time*, in this case, set equal to $4ms$. Multiple triggers may occur for the same pixel within a single laser pulse, in case of very bright particles. Such occurrences are treated the same as once-activated pixels. Specifically, the obtained pseudo-snapshots are binary, with pixel

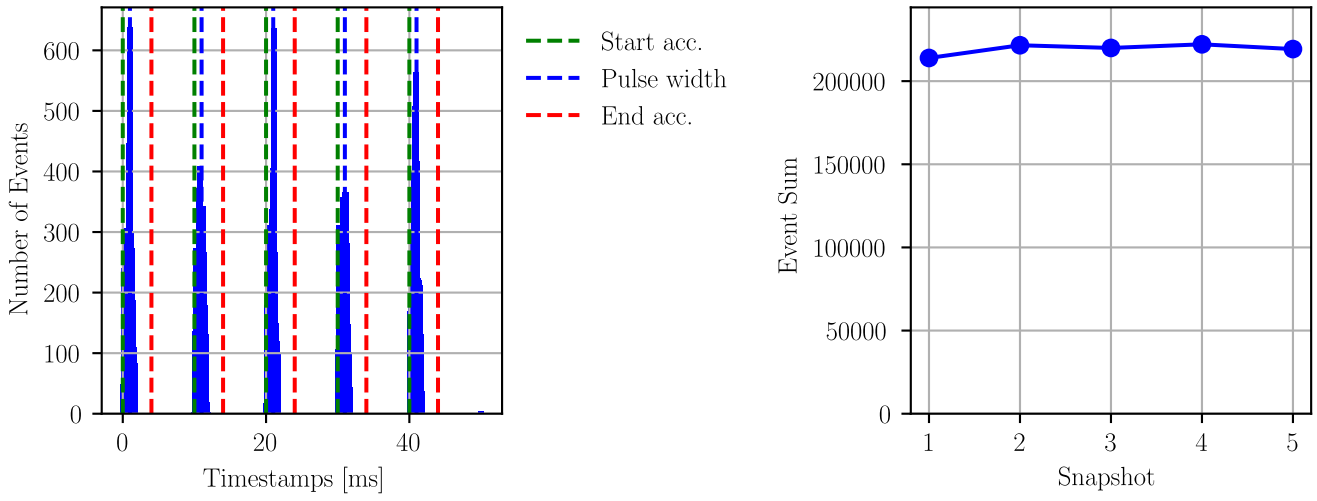

Figure 2. Example of event-rate from EBV camera with pulsating laser. On the left, a histogram with the event bursts related to five laser pulses. Green, blue and red dashed lines indicate respectively the beginning and end of the laser pulse, and the end of the accumulation time. On the right, the number of events finally accumulated for 4 pseudo-snapshots.

values of 0 indicating no activation and 1 indicating that the pixel was activated at least once. The resulting synthetic images are subsequently subjected to a convolutional filter aimed at removing single-pixel activation related to noisy events, followed by Gaussian smoothing with a kernel size of 1. The latter is applied considering that the synthetic snapshots will be processed using standard PIV algorithms.

To ensure a fair comparison, it is crucial that both the PIV and EBIV datasets have the same resolution, denoted as Res. Careful positioning of both cameras was undertaken to achieve the closest possible resolution. The resulting values for the conventional PIV camera and the EBV camera are $Res_{\mathrm{PIV}} = 9.25\,\mathrm{pixel/mm}$ and $Res_{\mathrm{EBIV}} = 9.13\,\mathrm{pixel/mm}$, respectively.
In Fig. 3 one example of a snapshot used for PIV algorithm processing for the two acquiring technologies is shown. The pseudo-snapshot from the EBV camera (on the right) has already been filtered as previously described. Cumulative minimum background removal was applied to the snapshot from the conventional PIV camera.

The two sets of raw images were processed using PaIRS (Astarita & Cardone, 2005; Astarita, 2006; Paolillo & Astarita, 2024), an open-access PIV code from Università Federico II di Napoli. In both instances, an iterative multi-grid/multi-pass image deformation algorithm was employed, using final interrogation windows with dimensions of $32 \times 32\,\mathrm{pixel}$ and a 75% relative overlap. In both cases, the velocity fields have been post-processed using a Savitzky–Golay filter, with a square window of size of 5×5 grid points.

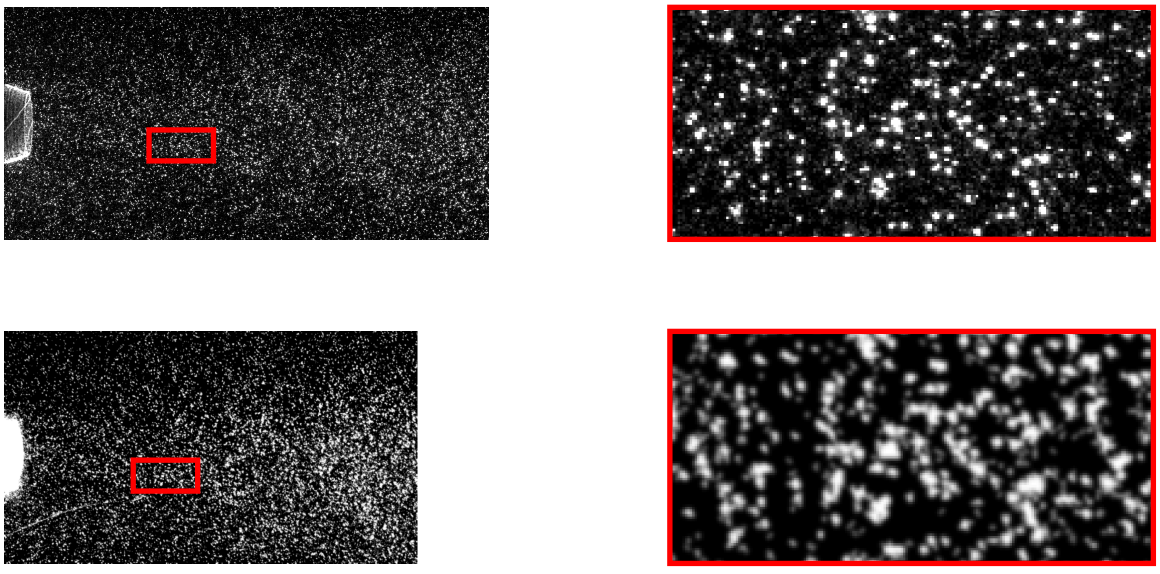

Figure 3. Comparison of input images for PIV processing: conventional PIV camera image (top) and EBV camera pseudo-snapshot (bottom). On the left, the full field of view. On the right, the zoomed red squared area. Both images corresponds to the same laser pulse and have undergone preprocessing.

3. Results

For the sake of comparison, the obtained velocity fields are interpolated onto a common grid, spanning $0.5 \leq x/D \leq 6.5$ and $-1.75 \leq y/D \leq 1.75$, shown as the red dashed box in fig. 1 (bottom). Since the focus is on mode extraction with POD, interpolation artefacts are expected to affect mostly high-order modes, thus without any significant effect on the analysis to be carried out here.

3.1. Flow statistics and spectra

Velocity profile statistics are reported in Fig. 4. In both cases, the velocities are normalized by the center-line velocity U_c in the core of the jet, at the location of the statistics $x/D = 2$. Very good agreement is observed between the two measurements. The main discrepancy in EBIV pertains to

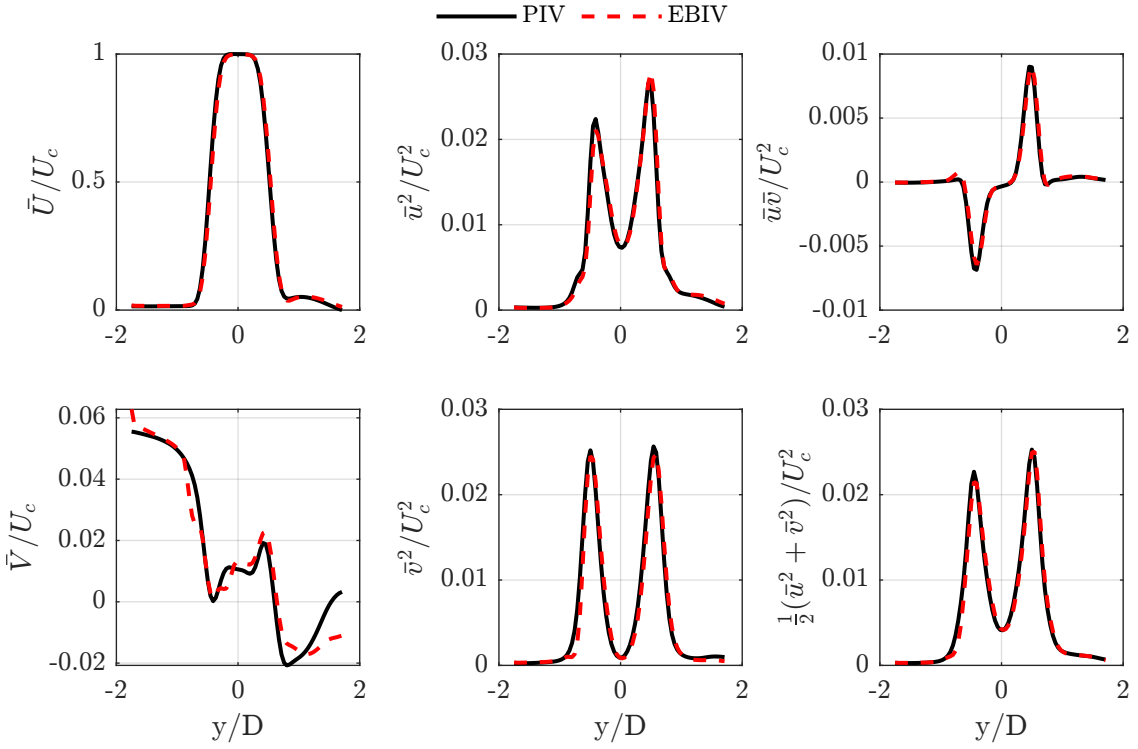

Figure 4. Statistics comparison between the conventional PIV (black line) and the EBV (dashed red line) cameras results. Statistics are plotted at the longitudinal location $x/D = 2$.

the average radial velocity component $\bar{V}$, which exhibits an offset compared to the PIV result. Considering that the order of magnitude of this component is significantly smaller than the streamwise one, this effect might be ascribed to uncertainty in the alignment.

A notable difference between the two measurements is observed in the power spectral density (PSD) in time of the velocity components. Fig. 5 illustrates the behaviour of the PSD of the fluctu-

ating component of the axial velocity u in the flow domain. Analogous results have been observed for the radial component v. The comparison between PIV and EBIV is shown in two specific points in the two top plots highlighted in red (b,c). The PSDs are computed at the grid points with coordinates ($x/D = 2$, $y/D = 0$) and ($x/D = 5$, $y/D = 0.5$), located in the jet core and shear layer, respectively, as indicated by the red diamonds in the top image.Good agreement is observed in the frequency range $St < 1.5$, where the Strouhal number St is obtained normalizing the frequencies by the nozzle diameter D and the jet bulk velocity U_j. At both points, EBIV exhibits different behavior for frequencies associated with $St > 1.5$, but with opposite trends in the two regions of the jet. In the core, the energy is significantly higher at higher frequencies, whereas within the shear layer, it is lower. This difference can be attributed to the higher noise level in the pseudo-images generated from the EBV camera data stream. The noise, not tied to any specific frequency, is distributed across the entire spectrum, resulting in the core in a higher plateau reflecting its intensity. This occurs because the core area is primarily dominated by the shedding frequency of the jet vortex rings. In contrast, the shear layer is characterized by a broadband turbulent spectrum. The different behavior in the shear layer is ascribed to a higher number of outliers detected during the EBIV processing and their subsequent removal, leading to lower energy content.

The maps displayed in the other plots of the figure are generated by calculating the PSD at each grid point along lines parallel to the x-direction, specifically at $y/D = 0$ (d,e) and $y/D = 0.5$ (f,g). These lines are depicted on the velocity map with black and cyan dashed lines, respectively, and the maps are outlined with corresponding color-coded frames. Results from PIV are shown on the left (d,f), while those from EBIV are presented on the right (e,g).

In general, the characteristics observed in the single-point PSD hold true for the entire flow domain. The most energetic frequencies are accurately described by EBIV, both in the shear and core regions. However, for $St > 1.5$, corresponding to frequencies $f > 10\,\text{Hz}$, significant differences arise: higher PSD values are observed in the core, while attenuation at higher frequencies occurs in region of high turbulence. The latter trend is evident throughout the maps related to the line $y/D = 0.5$, and in the case of $y/D = 0$ for $x/D \geq 4$, corresponding to the core collapse.

3.2. Modal analysis

A modal analysis has been performed via POD, using the snapshot method by Sirovich (1987). Spatial and temporal modes, columns of the resulting matrices Φ and Ψ respectively, and singular values, diagonal elements in Σ, are computed on the overall set of $4{\cdot}10^4$ snapshots for both the PIV and EBIV experiments.

Figure 6 presents the mode energy results derived from the square of their singular values, s. In both plots, each sequence is normalized by the cumulative sum of the squared singular values specific to that technique, i.e., PIV or EBIV. The left plot compares the normalized squared singular

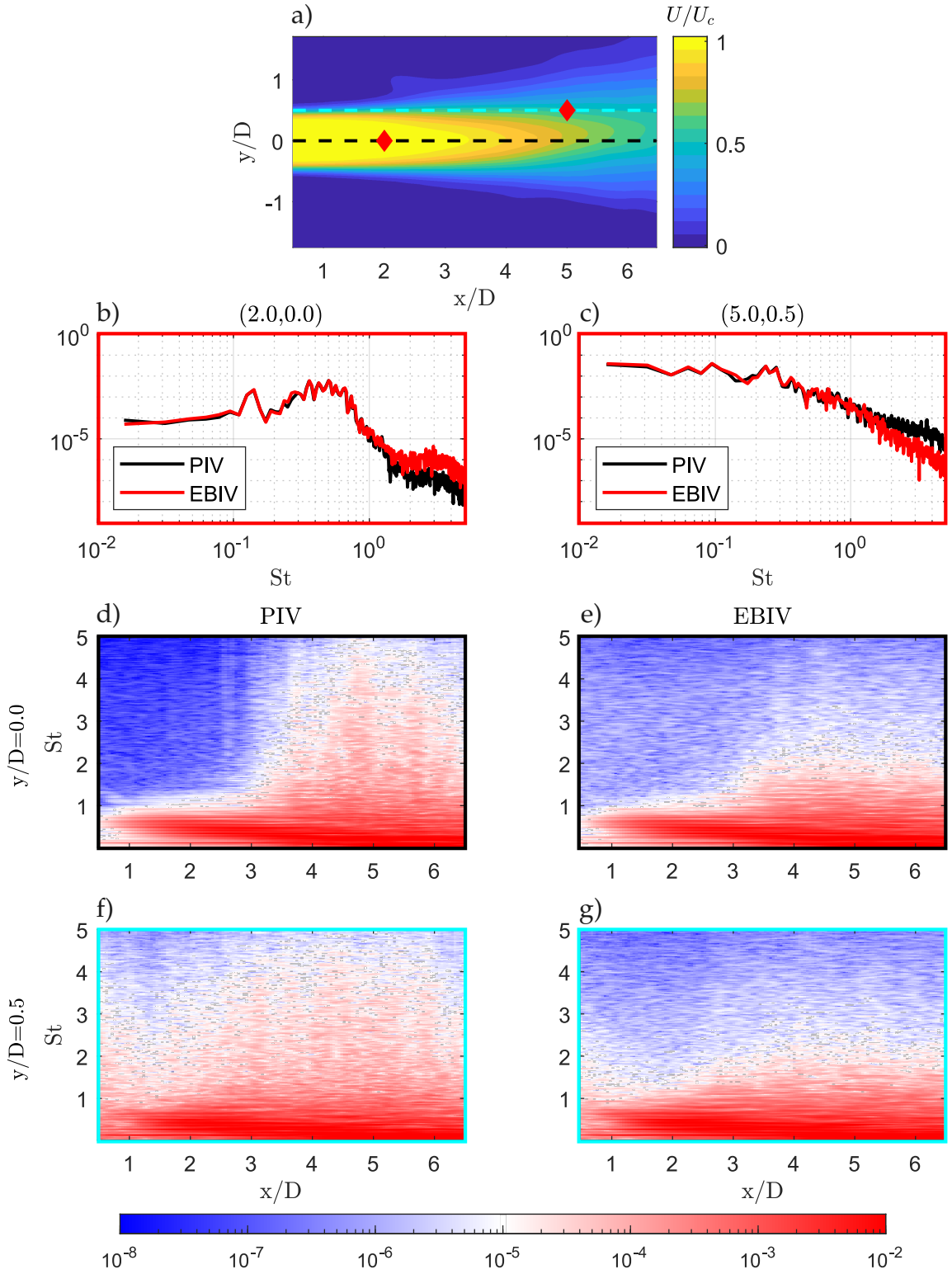

Figure 5. Power Spectral Density (PSD) of the u velocity component of the jet flow. The red box highlights the comparison between the two measurements in the core (b) and in the shear layer (c). The locations are indicated in the top plot with red diamonds and the coordinates are shown on top of the plots. The black (d,e) and cyan (f,g) boxes represent the PSD maps along the lines $y/D = 0$ and $y/D = 0.5$, respectively, as shown in the top plot. On the left (d,f) are the results from PIV, while on the right (e,g) are those from EBIV.

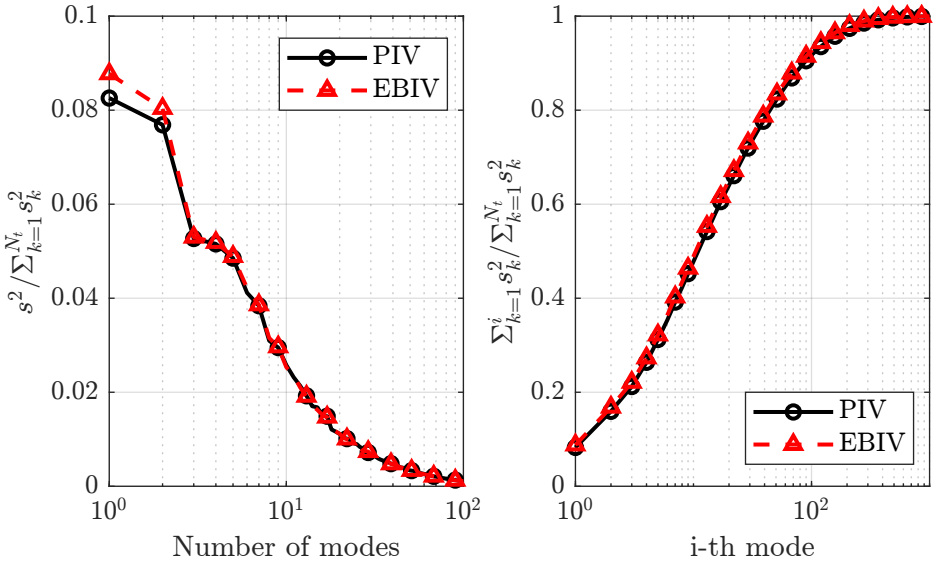

Figure 6. Mode energy comparison: energy associated with each mode (left) and cumulative energy(right), normalized by the total energy of the specific measurement technique. In black the results from PIV measurement, in red from EBIV. For sake of visualization only the first 10^2 modes on the left and 10^3 on the right are shown.

values between the two measurement techniques. The trend is accurately captured by EBIV, as also illustrated in the plot on the right, which shows the cumulative sum of the squared singular values up to the i-th mode. In this case, EBIV tends to overestimate the energy associated with the first few modes, as evidenced by a slightly higher total turbulent kinetic energy compared to PIV. This difference is likely to be attributed to a misalignment between the two analyzed flow fields. The observed discrepancy is specific to these measurements and cannot be generalized or ascribed to the measurement technique itself, not being observed consistently by the authors in other experimental datasets. The relative difference in the total turbulent kinetic energy, however, is rather small, approximately summing to a 3%.

To examine the convergence of the two measurements to the reference value established by the POD results on the overall dataset, random batches of snapshots were chosen from the original dataset, and the POD process was reiterated. Different batch sequences were tested, showing consistent behavior. The convergence analysis is presented in Fig. 7 in terms of the square of the singular values obtained. The dashed lines with markers represent the reference values obtained over the full dataset. For the sake of visualization, only two cases are shown, considering 500 snapshots on the left, and 1500 on the right. Despite a small systematic discrepancy between PIV and EBIV on the total kinetic energy of the flow, the convergence to the reference value aligns with that of PIV, if not faster. Specifically, EBIV results demonstrate good convergence after approximately 1500 snapshots, similar to what was obtained for PIV.

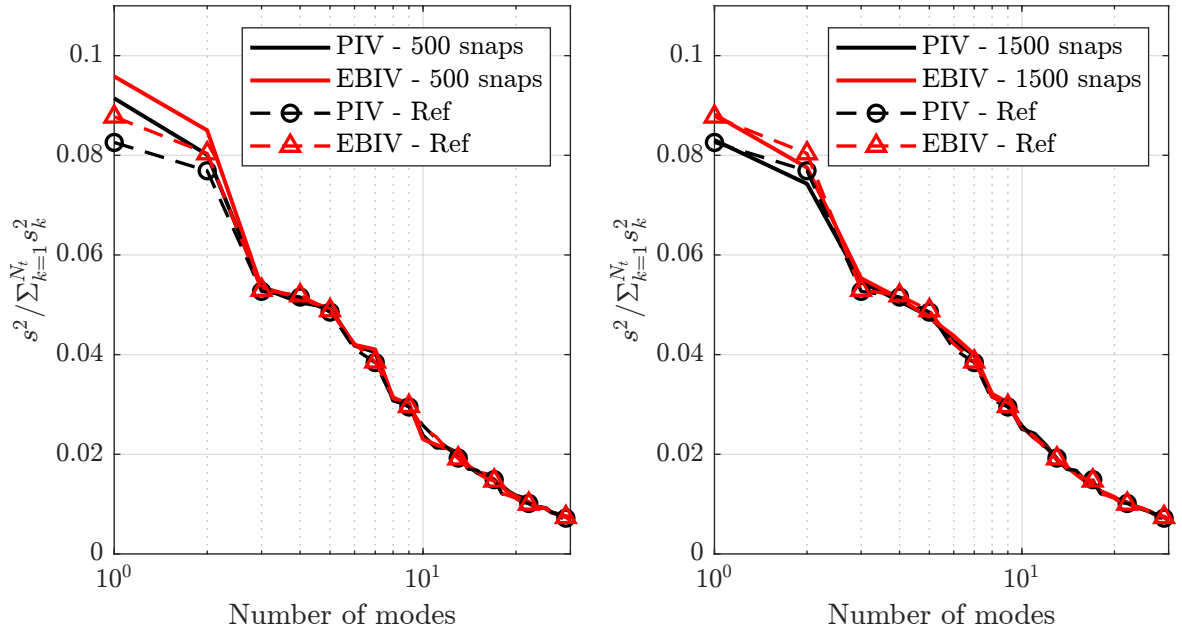

Figure 7. Modes energy convergence considering 500 (on the left) and 1500 (on the right) snapshots, represented with continuous lines. The results from PIV measurements are shown in black, and those from EBIV are shown in red. The reference "Ref", in dashed lines and with markers, pertains to the values obtained over the full dataset. The markers are distributed logarithmically and only the first 30 modes are shown.

The synchronized experiment enabled a comparison of the temporal modes obtained by the two measurement techniques. This result is crucial for flow control purposes as it addresses whether EBV technology can capture the same flow dynamics as conventional PIV cameras, thus allowing real-time reaction to flow changes. For this purpose, a common spatial basis was established, and the velocity results were projected onto it. Specifically, the product between spatial basis and singular values from PIV measurement $\Phi_{\text{PIV}}\Sigma_{\text{PIV}}$ was set as basis. For both measurements, the projected temporal modes were obtained as:

$$\Psi_{(\cdot),\text{proj}} = (\Sigma_{\text{PIV}}^{-1}\Phi_{\text{PIV}}^{T}U_{(\cdot)})^{T} = U_{(\cdot)}^{-1}\Phi_{\text{PIV}}\Sigma_{\text{PIV}} \qquad \text{where } (\cdot) = \{\text{ PIV, EBIV}\} \tag{2}$$

where U is a $2N_p \times N_t$ real-value matrix containing the velocity fluctuations in the N_p grid points for all obtained snapshots N_t.

The results are shown in fig. 8 for different modes. The values of the projected temporal modes $\Psi_{(\cdot),\text{proj}}$ are normalized by the squared root of the number of snapshots N_t. Even for the higher mode number, typically subjected to noise corruption, EBIV demonstrates its capability to accurately describe the same dynamics as PIV.

More generally, assuming the PIV results as the ground truth, the normalized root mean square error (RMSE) between the i-th EBIV and PIV modes can be introduced. This error is defined for the temporal and spatial modes, respectively, as follows:

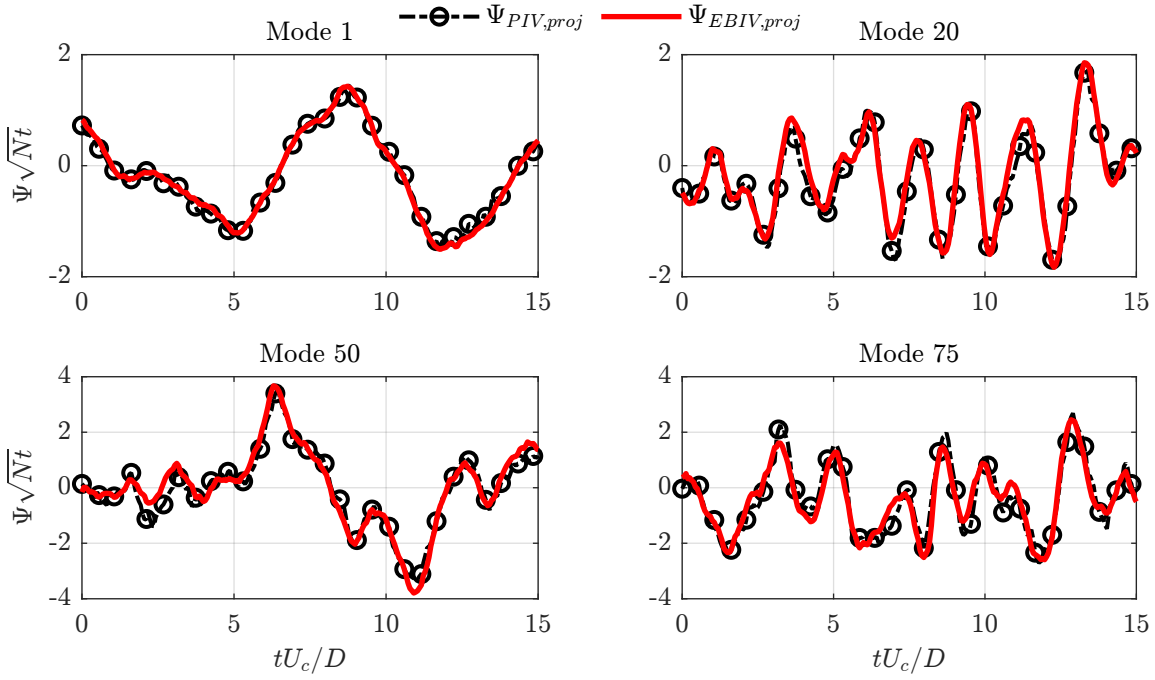

Figure 8. Projection of the temporal modes 1, 20, 50 and 75 onto a common spatial basis ($\Phi_{\text{PIV}}\Sigma_{\text{PIV}}$ in this case), for 15 convective time units. In dashed black line with markers the results from PIV. In red the result from EBIV.

$$\epsilon_{\psi,i} = \sqrt{\frac{\sum_{j=1}^{N_t} \left(\psi_{\text{PIV},i}(j) - \psi_{\text{EBIV},i}(j)\right)^2}{N_t}} \qquad \epsilon_{\phi,i} = \sqrt{\frac{\sum_{j=1}^{2N_p} \left(\phi_{\text{PIV},i}(j) - \phi_{\text{EBIV},i}(j)\right)^2}{2N_p}} \tag{3}$$

It should be noted that for the temporal and spatial modes, the error is defined between the projected values onto a common basis: in this case, $\Phi_{\text{PIV}}\Sigma_{\text{PIV}}$ and $\Sigma_{\text{PIV}}\Psi_{\text{PIV}}^T$, respectively. The error definitions are not normalized. This is because the obtained modes have unitary norm. Thus, the RMSE between two unit-norm vectors already provides normalized results.
The errors are plotted in Fig. 9. ϵ_ψ and ϵ_ϕ are particularly small for the initial ones but progressively increase with the mode number due to the higher noise corruption typical of experimental data. Overall, EBIV accurately identifies spatial and temporal characteristics, demonstrating robustness to noise in the raw data and yielding results similar to PIV even at higher mode numbers. The main discrepancy lies in the estimation of the singular values of the most energetic modes (see fig. 6), with an error of about 10% compared to the PIV values.

Finally, a Low Order Reconstruction (LOR) is computed by considering only the first r modes from the POD. An increasing rank r is considered, and the obtained LORs are compared between PIV and EBIV. This comparison allows for evaluating the dimensionality reduction capabilities of EBIV. To this aim, a specific error metric is defined, which can be related to the average spatial error $\epsilon_{LOR,sp}$ or the average temporal error $\epsilon_{LOR,t}$. In the first case, the point-wise difference between the two LOR velocity fluctuation fields is averaged over all reconstructed snapshots (N_t), resulting in an error map (shown in Fig. 10, left, for $r = 50$). In the second case, $\epsilon_{LOR,t}$ is obtained as the average

of the point-wise differences over each snapshot, yielding an error value for each snapshot.

$$\epsilon_{\text{LOR,sp}} = \frac{1}{TKE_{\max}} \sqrt{\frac{\sum_{j=1}^{N_t} \left(u_{\text{PIV},j} - u_{\text{EBIV},j}\right)^2}{N_t}} \qquad \epsilon_{\text{LOR,t}} = \frac{1}{TKE_{\max}} \sqrt{\frac{\sum_{j=1}^{2N_p} \left(u_{\text{PIV},j} - u_{\text{EBIV},j}\right)^2}{2N_p}} \tag{4}$$

Both the error definitions are normalized by the maximum value of the mean turbulent kinetic energy measured with PIV.

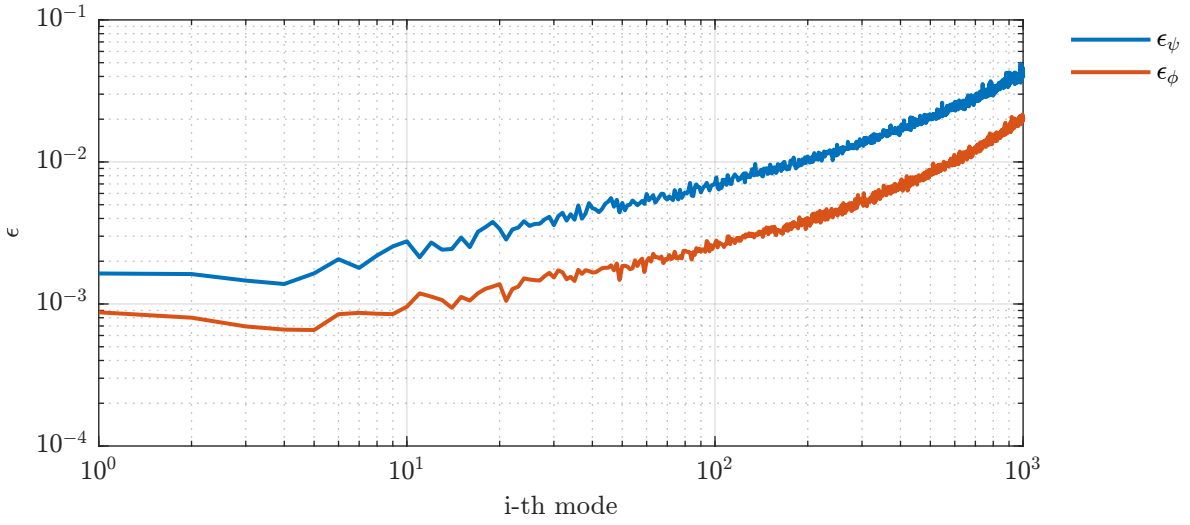

Figure 9. Root mean square error of the projected temporal ψ (in blue) and spatial modes ϕ (in red) over common basis. In dashed yellow line the RMSE related to the singular values σ. The first 10^3 modes are shown.

For each chosen LOR rank, both an error map and a time series of the reconstruction error are obtained. An overall LOR error can then be evaluated by averaging the error map ($\epsilon_{LOR,sp}$) or the time series ($\epsilon_{LOR,t}$), resulting in $\delta_{LOR,sp}$ and $\delta_{LOR,t}$, respectively. The obtained values are reported in the plot on the right of fig.10.

Similarly to the mode errors, δ increases with the inclusion of a higher number of modes in the LOR, due to their corruption. The error map $\epsilon_{LOR,sp}$ on the left indicates that the primary discrepancies occur downstream of the jet ($x/D > 4$), which coincide with the region of peak turbulent kinetic energy. Considering also the differences highlighted in the spectrum analysis, EBIV struggles more in accurately reconstructing broad-spectrum turbulent regions. Nonetheless, the discrepancies are minor—within a few percentage points—and remain acceptable for flow control applications.

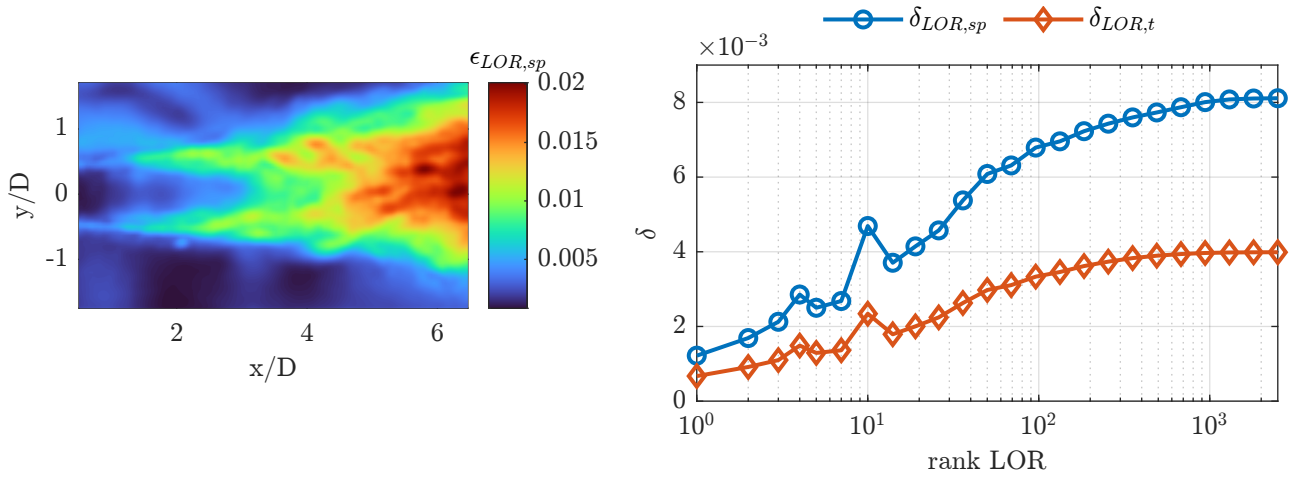

Figure 10. Low Order Reconstruction (LOR) error. On the left, the error map $\epsilon_{\mathrm{LOR,sp}}$ obtained for LOR-rank $r = 50$. On the right, the overall errors $\delta_{\mathrm{LOR,sp}}$ and $\delta_{\mathrm{LOR,t}}$ for different rank values. Values up to $r = 2.5{\cdot}10^3$ are shown.

4. Conclusions

This study has explored the viability of utilizing neuromorphic event-based vision (EBV) cameras for low-order modelling, which is of great relevance for flow control. The assessment was conducted on a jet experiment, using standard PIV as a benchmark.

The results indicate that EBV cameras can achieve comparable flow statistics to conventional PIV ones. Slight discrepancies seem likely to be due to alignment issues. Spectral analysis revealed that EBV cameras accurately capture the most energetic frequencies in the flow domain, though with some differences in the higher frequency range. This variance can be attributed to the noise levels inherent in the EBV data and the specific processing algorithms, derived from conventional PIV approaches.

The modal analysis via POD demonstrated that EBV cameras can successfully identify the dominant flow structures and their associated energies. Despite an overestimation of the energy in the first few modes, the overall energy distribution and convergence of EBIV were comparable to those obtained with PIV. This suggests that EBIV is capable of providing a reliable basis for reduced-order modeling of flow dynamics.

Moreover, the projection of temporal modes onto a common spatial basis confirmed that EBIV capture flow dynamics similar to PIV, which is crucial for applications in real-time flow control. Good agreement is found also in the obtained low-order reconstructions

It is important to highlight that PIV ad-hoc algorithms and experimental setup have been implemented, albeit applied to a novel technology. The authors believe that developing a dedicated event-based data-processing framework and fine-tuning the experimental setup can significantly

enhance the measurement quality.

In conclusion, this study highlights the promising capabilities of EBV cameras in the field of flow diagnostics and control. Despite challenges such as noise levels and event rate constraints, the significant reduction in data volume, enhanced sensor sensitivity, and innovative data representation make EBIV a strong candidate for real-time, imaging-based applications. Future work will focus on developing proper algorithms to better leverage the unique capabilities of event-based cameras, exploring a broader range of fluid dynamics applications and the integration of EBV cameras in closed-loop control systems .

Acknowledgment

This project has received funding from the European Research Council (ERC) under the European Union's Horizon 2020 research and innovation program (grant agreement No 949085). Views and opinions expressed are however those of the authors only and do not necessarily reflect those of the European Union or the European Research Council. Neither the European Union nor the granting authority can be held responsible for them.

References

Astarita, T. (2006). Analysis of interpolation schemes for image deformation methods in piv. *Experiments in fluids*, *40*, 977–987.

Astarita, T., & Cardone, G. (2005). Analysis of interpolation schemes for image deformation methods in piv. *Experiments in fluids*, *38*, 233–243.

Gallego, G., Delbrück, T., Orchard, G., Bartolozzi, C., Taba, B., Censi, A., ... Scaramuzza, D. (2022). Event-based vision: A survey. *IEEE Transactions on Pattern Analysis and Machine Intelligence*, *44*(1), 154-180. doi: 10.1109/TPAMI.2020.3008413

Lichtsteiner, P., Posch, C., & Delbruck, T. (2008). A 128×128 120 dB 15 μs latency asynchronous temporal contrast vision sensor. *IEEE Journal of Solid-State Circuits*, *43*(2), 566-576. doi: 10.1109/JSSC.2007.914337

Lumley, J. (1967). The structure of inhomogeneous turbulent flows. *Atmospheric Turbulence and Radio Wave Propagation*, 166-178. Retrieved from `https://cir.nii.ac.jp/crid/1574231874542771712`

Paolillo, G., & Astarita, T. (2024, July 08–11). Pairs-unina: A robust and accurate free tool for digital particle image velocimetry and optical camera calibration. In *Proceedings of 21st international symposium on applications of laser and imaging techniques to fluid mechanics.* Lisbon, Portugal.

Posch, C., Serrano-Gotarredona, T., Linares-Barranco, B., & Delbruck, T. (2014). Retinomorphic event-based vision sensors: Bioinspired cameras with spiking output. *Proceedings of the IEEE*, *102*(10), 1470-1484. doi: 10.1109/JPROC.2014.2346153

Rusch, A., & Rösgen, T. (2023). TrackAER: real-time event-based quantitative flow visualization. *Experiments in Fluids*, *64*(8).

Shiba, S., Hamann, F., Aoki, Y., & Gallego, G. (2023). Event-based background-oriented schlieren. *IEEE Transactions on Pattern Analysis and Machine Intelligence*, 1-16. doi: 10.1109/TPAMI.2023.3328188

Siegel, S., Cohen, K., McLaughlin, T., & Myatt, J. (2003). Real-time particle image velocimetry for closed-loop flow control studies. In *41st Aerospace Sciences Meeting and Exhibit.* Retrieved from `https://arc.aiaa.org/doi/abs/10.2514/6.2003-920` doi: 10.2514/6.2003-920

Sirovich, L. (1987). Turbulence and the dynamics of coherent structures. i. coherent structures. *Quarterly of applied mathematics*, *45*(3), 561–571.

Wang, Y., Idoughi, R., & Heidrich, W. (2020). Stereo event-based particle tracking velocimetry for 3d fluid flow reconstruction. *Computer Vision – ECCV 2020*, 36–53.

Willert, C. (2023). Event-based imaging velocimetry using pulsed illumination. *Experiments in Fluids*, *64*, 98. doi: 10.1007/s00348-023-03641-8

Willert, C., Munson, M., & Gharib, M. (2010). Real-time particle image velocimetry for closed-loop flow control applications. *Conference Proceedings of 15th International Symposium on Applications of Laser Techniques to Fluid Mechanics*, *Lisbon, 5-8 July 2010.*.